Acta Oceanol. Sin., 2022, Vol. 41, No. 9, P. 117–126
https://doi.org/10.1007/s13131-022-2003-7
http://www.aosocean.com
E-mail: ocean2@hyxb.org.cn

Control of the stress field on shallow seafloor hydrothermal paths: A case study of the TAG hydrothermal field

Mingxu Wang[1, 2], Chunhui Tao[2, 3, 1]*, Chao Lei[4], Hanchuang Wang[2, 3], Ming Chen[1]

[1] School of Oceanography, Shanghai Jiao Tong University, Shanghai 200030, China

[2] Key Laboratory of Submarine Geosciences, Ministry of Natural Resources, Hangzhou 310012, China

[3] Second Institute of Oceanography, Ministry of Natural Resources, Hangzhou 310012, China

[4] College of Marine Science and Technology, China University of Geosciences, Wuhan 430074, China

Received 1 February 2021; accepted 5 February 2022

Abstract

The stress state and rock mechanical properties govern the growth of faults and fractures, which constitute shallow hydrothermal pathways and control the distribution of seafloor massive sulfide (SMS) mounds in the seafloor hydrothermal field. The stress field has an important influence on the formation and persistence of hydrothermal pathways. Based on multibeam bathymetric data from the Trans-Atlantic Geotraverse (TAG) field, we establish two three-dimensional geological models with different scales to simulate the stress field, which investigate the characteristics of hydrothermal pathways and associated SMS mounds. The simulation results show that oblique faults and fissures form in the tensile stress zone and that mounds, including active and inactive hydrothermal mounds form in the compressive stress zone. Fault activity, which is related to the stress field, affects the opening and closing of hydrothermal channels and changes the permeability structure of subseafloor wall rock. Therefore, the stress field controls the development and persistence of shallow hydrothermal pathways. The features of shallow hydrothermal pathways in the stress field can provide geomechanical information that is useful for identifying favorable zone for SMS deposit formation.

Key words: stress field, hydrothermal paths, TAG hydrothermal field, numerical modelling

Citation: Wang Mingxu, Tao Chunhui, Lei Chao, Wang Hanchuang, Chen Ming. 2022. Control of the stress field on shallow seafloor hydrothermal paths: A case study of the TAG hydrothermal field. Acta Oceanologica Sinica, 41(9): 117–126, doi: 10.1007/s13131-022-2003-7

1 Introduction

Seafloor massive sulfide (SMS) deposits are mainly discovered at ocean spreading ridges and are commonly seen as future deep-sea resources (Hannington et al., 2011; German et al., 2016; Petersen et al., 2016). The abundance of SMS deposits in neovolcanic zones of global oceans is estimated at 6×10^8 t, and tectonic-hosted SMS deposits exhibit high concentrations of Cu and Au with high commercial interest (Hannington et al., 2011; German et al., 2016; Petersen et al., 2016). However, mining of SMS deposits is suggested to be restricted to inactive SMS deposits. Koschinsky et al. (2018) and Jamieson and Gartman (2020) proposed the concept of geological connectivity to define hydrothermal activity at the vent field scale, containing hydrothermal circulation cells. Understanding the formation of hydrothermal vents is key for defining hydrothermal activity and classifying SMS deposits, as hydrothermal activity and SMS deposits require heat sources, hydrothermal fluids, and channels (Tivey, 2007; Olive and Crone, 2018). Shallow subcirculating fluid channels control the locus of hydrothermal fluids venting on the seafloor (Sleep, 1991), and faults and fissures within the oceanic crust provide hydrothermal paths, which determine the location of hydrothermal activity and SMS deposits on the seafloor (Kleinrock and Humphris, 1996; Bohnenstiehl and Kleinrock, 2000; Carruthers et al., 2013). Dike emplacement changes the stress state and provides a damage zone with high permeability (Bohnenstiehl and Kleinrock, 2000; Germanovich et al., 2000). Additionally, numerical simulations have revealed that the stress field is one of the important factors affecting the development of faults and fissures (Eshiet et al., 2018; Chen et al., 2020) and that the permeability of serpentinites with higher porosities is more sensitive to stress (Falcon-Suarez et al., 2017). Therefore, we propose that the stress field might influence the development and permeability of hydrothermal paths in a hydrothermal field.

Knowledge of the stress field has significant implications for the interpretation of the geodynamic process, management of georeservoirs and identification of geological repositories (Heidbach et al., 2018). The World Stress Map (WSM) project compiles global crustal stress state records, resolving stress pattern heterogeneities from plate-wide to local scales (Heidbach et al., 2018). Deriving the 3-D stress field from pointwise data is a key challenge for investigators, and geomechanical numerical models have been set up for predicting the present-day stress

Foundation item: The National Natural Science Foundation of China under contract No. 42127807; the Key R&D Program of Zhejiang Province under contract No. 2021C03016; the National Key R&D Program of China under contract No. 2017YFC0208401; the Oceanic Interdisciplinary Program of Shanghai Jiao Tong University under contract Nos SL2020MS033, SL2020ZD205 and SL2104; the Scientific Research Fund of Second Institute of Oceanography under contract Nos SL2020MS033, SL2020ZD205 and SL2104; the Talent Cultivation Project of Zhejiang Association for Science and Technology under contract No. SKX201901.
*Corresponding author, E-mail: taochunhuimail@163.com

field in the Australian continental crust and analysing the stress state of faults and petroleum accumulation in basins (Hergert and Heidbach, 2011; Rajabi et al., 2017; Hu et al., 2019). However, the stress database primarily contains the stress tensor rotation, and very few or even no data are available for small-scale models (Heidbach et al., 2018). Previous researchers have made successful attempts to derive the topographic stress field and found that topographic stress can influence subsurface rock fracture patterns (Slim et al., 2015). Furthermore, geological data reveal the control that topographic stress has on bedrock weathering and hydrothermal vent occurrence (Schöpa et al., 2011; Clair et al., 2015; Chen et al., 2017). However, the precise relationship between the stress field and hydrothermal paths is not well understood.

The Trans-Atlantic Geotraverse (TAG) hydrothermal field has been intensively studied (Murton et al., 2019), as the detachment fault has been exploited to extract heat from a deep melt reservoir (deMartin et al., 2007). Faults control the localization of hydrothermal activity at the active TAG mound (Kleinrock and Humphris, 1996), furthermore, the properties of the faults and fissures there suggest a relationship between the stress field and hydrothermal venting (Bohnenstiehl and Kleinrock, 2000). The geophysical records imply that there are fluid subreservoirs and secondary circulation systems distributed beneath the hydrothermal field (Sohn et al., 2009; Pontbriand and Sohn, 2014). To better understand the control of the stress field on shallow seafloor hydrothermal paths, we establish two 3-D geomechanical models of different sizes to simulate the stress state of the TAG hydrothermal mound and field using multibeam bathymetric topographic data. The goal of the present study is to discuss the relationship among the stress field, hydrothermal vents, and shallow seafloor hydrothermal paths of the region.

2 Geological setting

The TAG hydrothermal field is one of the most intensively studied seafloor hydrothermal systems. It is located along the Mid-Atlantic Ridge, which has a slow spreading rate (22 mm/a), an axial valley controlled by NNE–SSW-oriented faults and abyssal hills, and water depths of –3 380 m to –3 760 m (Fig. 1). This area hosts young neovolcanic (NV) areas and active and inactive hydrothermal mounds (White et al., 1998; Murton et al., 2019). The detachment fault in the TAG field provides a pathway for hydrothermal fluid, which extracts heat from a deep source (deMartin et al., 2007; Murton et al., 2019). Active and inactive mounds are located in the fault and fissure zone of the Mid-Atlantic Ridge and controlled by ridge-parallel (NNE-trending) and oblique faults and fissures (Kleinrock and Humphris, 1996; White et al., 1998; Bohnenstiehl and Kleinrock, 2000). The average depth of the fissures near the active TAG hydrothermal mound is approximately 70 m; the fissures have various strikes that differ from that of the ridge axis (Fig. 1b). Dyke intrusions formed these oblique fissures and maintained localized hydrothermal flow (Bohnenstiehl and Kleinrock, 2000). These fissures and faults can provide hydrothermal pathways for seawater entrainment and the ascent of hydrothermal flows (Humphris and Kleinrock, 1996; Humphris et al., 2015).

The faults parallel to the oceanic ridge (oriented NNE) and the oblique faults (oriented NWW) provide channels for hydrothermal fluid accumulation and release that form the TAG hydrothermal mound. The ascending hydrothermal fluid circulation

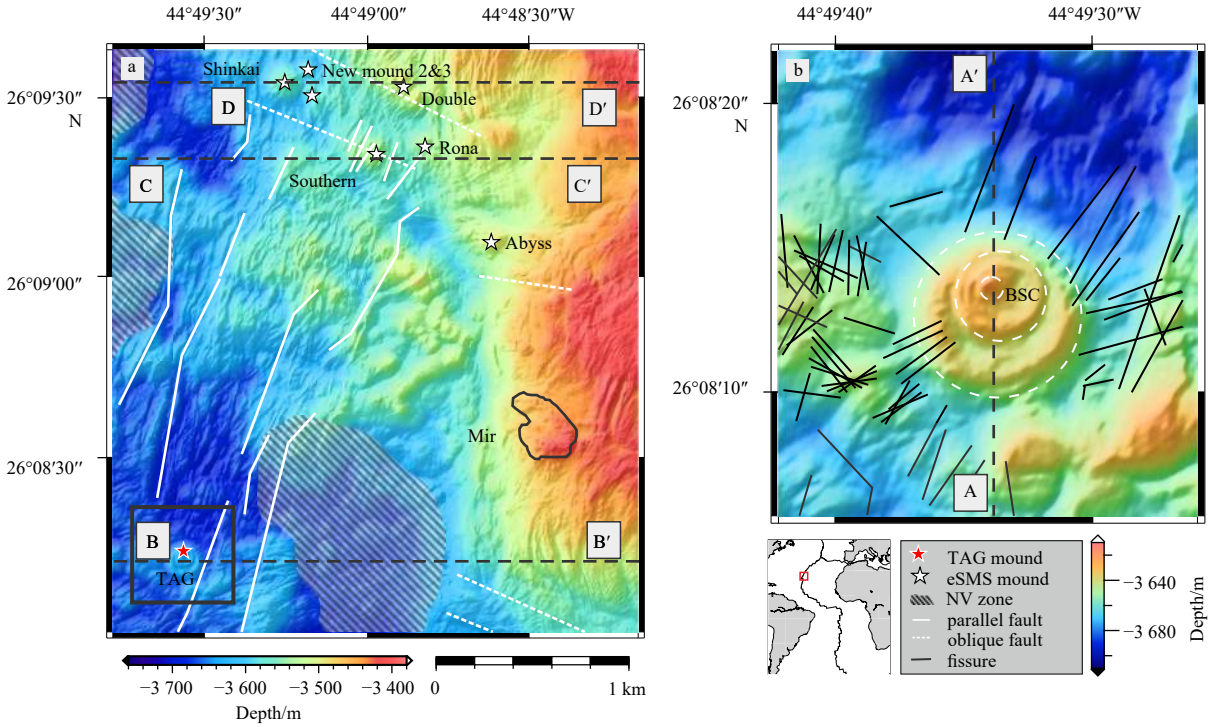

Fig. 1. Geological background of the TAG hydrothermal field (created with Generic Mapping Tools (GMT version 6) from https://www.generic-mapping-tools.org/). a. The red star represents the active TAG hydrothermal mound, the white stars show eSMS deposit mounds, white solid lines and dotted lines denote ridge-parallel faults and oblique faults, and shaded lines mark the young NV areas (modified from Murton et al. (2019)). The black rectangle indicates panel b. b. Topographic map of the TAG hydrothermal mound. The white dotted circles represent the scope and platform of the active TAG hydrothermal mound, the black smoker chimney (BSC) complex is in the middle circle, and the black solid lines denote fissures.

concentrates along the detachment fault, but the permeability structure of the seafloor largely determines the hydrothermal fluid release and the growth of chimneys (Humphris and Kleinrock, 1996; Kleinrock and Humphris, 1996; deMartin et al., 2007; Guo et al., 2020). Normal faults near the vent are conducive to hydrothermal circulation, and oblique faults that cross-cut the normal faults may control the location of the vent field on the seafloor (Grevemeyer et al., 2013). Pontbriand and Sohn (2014) proposed that microearthquakes 50–125 m beneath the subsurface of the active TAG mound are driven by volume expansion of anhydrite precipitated from the mixing of seawater and hydrothermal fluid (Pontbriand and Sohn, 2014). In addition, the abundant anhydrite in the summit and inner veins of the active TAG mound indicates that seawater was entrained into the shallow parts and stockworks of the mound (Humphris et al., 2015). Near-seafloor magnetic data reveal that nonmagnetic stockwork zones below the active TAG mound and extinct seafloor massive sulfide (eSMS) mounds are related to ascending hydrothermal pipes. The pipes beneath eSMS mounds are vertical, while those beneath the TAG mound dip 60° and trend N60°W (Tivey et al., 2003; Adelinet et al., 2013; Szitkar et al., 2019).

3 Finite element modelling

3.1 *Model assumptions*

Several stress sources contribute to the stress field on the following scales: First-order (>500 km) stress sources are the main plate boundary forces, and second-order (100–500 km) stress sources are the lithospheric variations. Third-order (<100 km) stress sources are local rock property differences, topography variations, and artificial stress disturbances (Reiter and Heidbach, 2014). Under the scale required to simulate the stress state of the TAG hydrothermal field, the model should be refined to reveal the topographic stress, thus we extract the geometric features from multibeam bathymetric data from the TAG hydrothermal field with a resolution of 2 m (Petersen, 2019). The plate boundary force of mid-ocean ridge spreading is represented by the displacement boundary condition, which previous researchers have applied (Reiter and Heidbach, 2014; Hu et al., 2019). Additionally, the pressure of the water column on the seafloor should not be neglected, and hydrostatic pressure is represented by the boundary load condition.

Linear elastic material properties are assumed in geomechanical numerical models (Schöpa et al., 2011; Griffith et al., 2014; Reiter and Heidbach, 2014; Chen et al., 2017), assigning the parameters to lithological layers. There are three groups of lineaments in the TAG area, which represent different stress regimes (Graber et al., 2020). The depths of the fissures near the active TAG mound is less than 500 m, with an average of 70 m (Bohnenstiehl and Kleinrock, 2000). Between 100 m and 125 m below the seafloor of the active TAG mound, the drilling core consists of altered basalt breccia (Grant et al., 2018), a microearthquake seismogenic zone of generally <150 m below the seafloor (Pontbriand and Sohn, 2014). Therefore, we assume that the thickness of the altered basalt breccia layer is 150 m near the TAG mound and 500 m in the TAG field.

As the description of the stress tensor in the WSM project, the three principal stresses (vertical stress S_V and the maximum and minimum horizontal stresses S_{Hmax} and S_{Hmin}) define the stress state at any point within a body (Heidbach et al., 2018); here, tensile stress is positive, the principal stresses σ_1 and σ_2 are horizontal, and the principal stress σ_3 is vertical (Schöpa et al., 2011).

3.2 *Model setup*

To investigate the implications of the stress field on hydrothermal paths, we establish a model of a TAG mound (Fig. 1b) to simulate the stress state of an active hydrothermal mound. Furthermore, we construct a model of the entire TAG field (Fig. 1a) as a comparison, examining the results of the former model. The models are illustrated in Fig. 2, and the scales are 500 m×554 m×H (Fig. 2a) and 3 001 m×3 325 m×H (Fig. 2b). We applied the Structural Mechanics module of COMSOL Multiphysics to solve the models. To eliminate the influence of the bottom boundary on the stress in the upper part of the model, the height H of the models is set to ten times the depth (Schöpa et al., 2011). The value of H is calculated by Eq. (1).

$$H = 10 \times (\mathrm{Depth}_{max} - \mathrm{Depth}_{min}) + \mathrm{Depth} - \mathrm{Depth}_{min}. \quad (1)$$

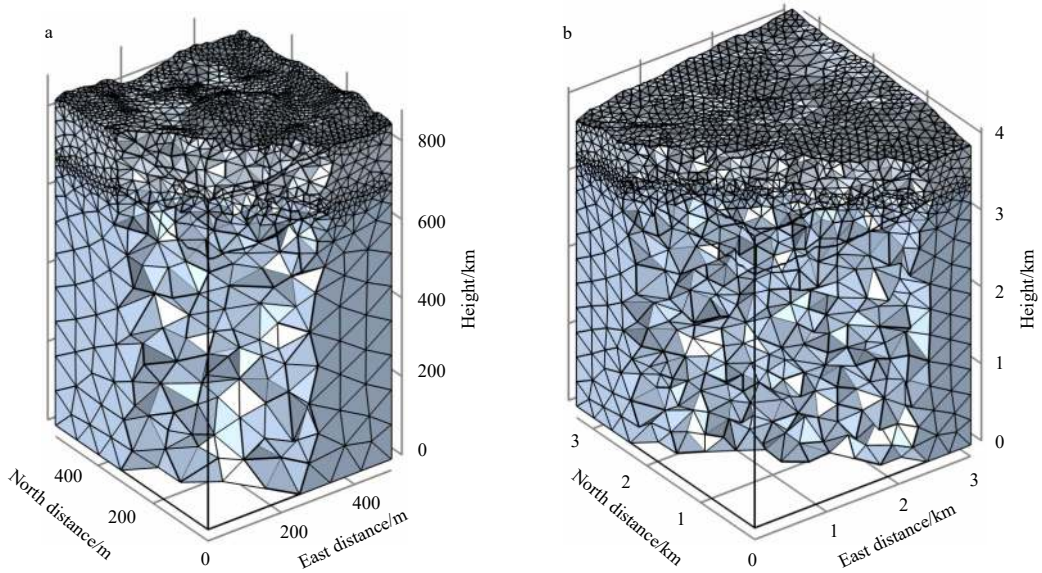

Fig. 2. Model A, 3-D geological model of the active TAG hydrothermal mound with a scale of 500 m×554 m×H (a); Model B, 3-D geological model of the TAG hydrothermal region with a scale of 3 001 m×3 325 m×H (b).

Based on drilling core and microearthquake evidence of cracking within the active TAG mound (Pontbriand and Sohn, 2014), the upper layer of altered oceanic crust consists of altered basalt breccia and mineral materials, with a thickness of 150 m in the mound. The crustal velocity model determines the inset detail panels for the eSMS mounds, the bottom boundary of the altered upper oceanic crust lies ~500 m below the seafloor, and the geometry is similar to the topography of the seafloor (Murton et al., 2019). Therefore, the thickness of the altered oceanic crust is 500 m in the TAG hydrothermal field. As shown in Fig. 2, the models are divided into two layers, and the petrophysical parameters of the materials are summarized in Table 1.

Vertical displacement should be zero at the lower boundary, except for the west boundary (Schöpa et al., 2011). In consideration of the spreading rate of the Mid-Atlantic Ridge, the normal displacement velocity of the west boundary is set at 13 mm/a (McGregor et al., 1977). Unlike geomechanical models without water body, the present-day stress field accounts for the ambient regional stress and the effects of the topography and seawater loading (Moon et al., 2020), and the external stress on the upper boundary is calculated with Eq. (2).

$$P_0 = g\int_0^Z \rho \mathrm{d}Z, \tag{2}$$

where P_0 is the external stress derived from surficial seawater loads, gravity g is 9.8 m/s^2, Z is the depth, and the density of water ρ is 1 000 kg/m^3.

Table 1. Petrophysical characteristics of each layer of rock (Hyndman and Drury, 1976; Chen et al., 2017)

Layer	Density/(kg·m^{-3})	Young's modulus/Pa	Poisson's ratio
Layer 1	2 795	7.740 6×10^{10}	0.295
Layer 2	2 975	1.072 1×10^{10}	0.310

The models are divided with a free tetrahedral mesh, as illustrated in Fig. 2. The size of Model A ranges from a minimum of 15.9 m to a maximum of 88.5 m, and 39 251 mesh cells are used. The size of Model B ranges from a minimum of 40.8 m to a maximum of 362 m, and 155 642 mesh cells are used. These two models are computed in a stationary solver based on the finite element method.

4 Results

Based on the convention that the tensile stress is positive, the principal stresses σ_1 and σ_2 are the maximum and minimum horizontal stresses, respectively, while the principal stress σ_3 is vertical. We present the results of the active TAG mound and TAG hydrothermal field. The magnitude of the maximum horizontal stress σ_1 is investigated to infer rock failure, and the magnitude of the vertical stress σ_3 is used to verify model reliability. In addition, the value of differential stress $\sigma_1-\sigma_3$ is adopted to evaluate fault activity.

Figure 3 shows the stress state of the active TAG mound. The domain of the TAG mound features a negative maximum horizontal stress σ_1, presenting a compressive stress zone (Fig. 3a). Fissures near the mound are mainly associated with positive maximum horizontal stress σ_1, presenting a tensile stress zone (Fig. 3a). The differential stress $\sigma_1-\sigma_3$ of the TAG mound is similar to the distribution of the maximum horizontal stress σ_1; the TAG mound is dominated by low differential stress, and the oblique fissures are mainly located in the region of high differential stress. The first row of Fig. 4 shows that the low-stress zone and high-stress zone are located on the TAG mound and fissure, respectively, with the maximum horizontal stress σ_1 (–25.65 MPa) at the dome of the TAG mound and the maximum σ_1 (29.94 MPa) at the outcrop with fissures (Figs 4a, d). The second row of Fig. 4 displays that the vertical principal stress σ_3 fluctuates at approximately 30 MPa and increases with depth, agreeing with the result of Eq. (2) (Figs 4b, e). The third row of Fig. 4 presents the differential stress inside Model A. The highest differential stress

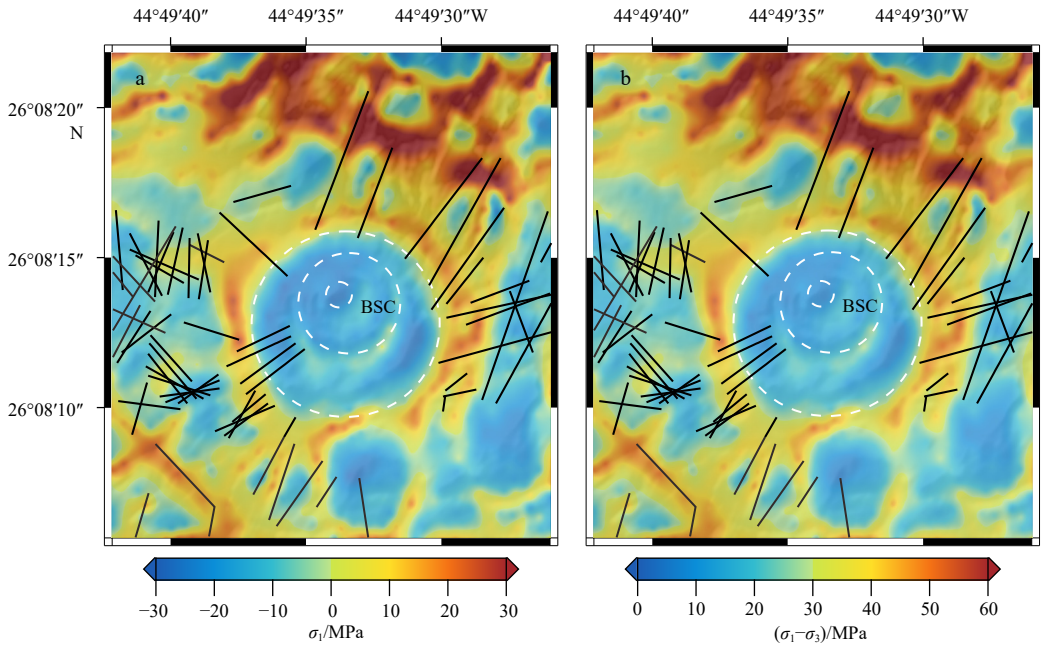

Fig. 3. Surface stress diagram of the 3-D geological model of the TAG active hydrothermal mound. a. The principal stress σ_1; b. the differential stress $\sigma_1-\sigma_3$. The white dotted circles in the figure represent the scope of the TAG active hydrothermal mound and the locations of black smoker chimneys (BSC). Solid black lines represent cracks near the TAG active hydrothermal mound, which are observed from near-bottom camera images.

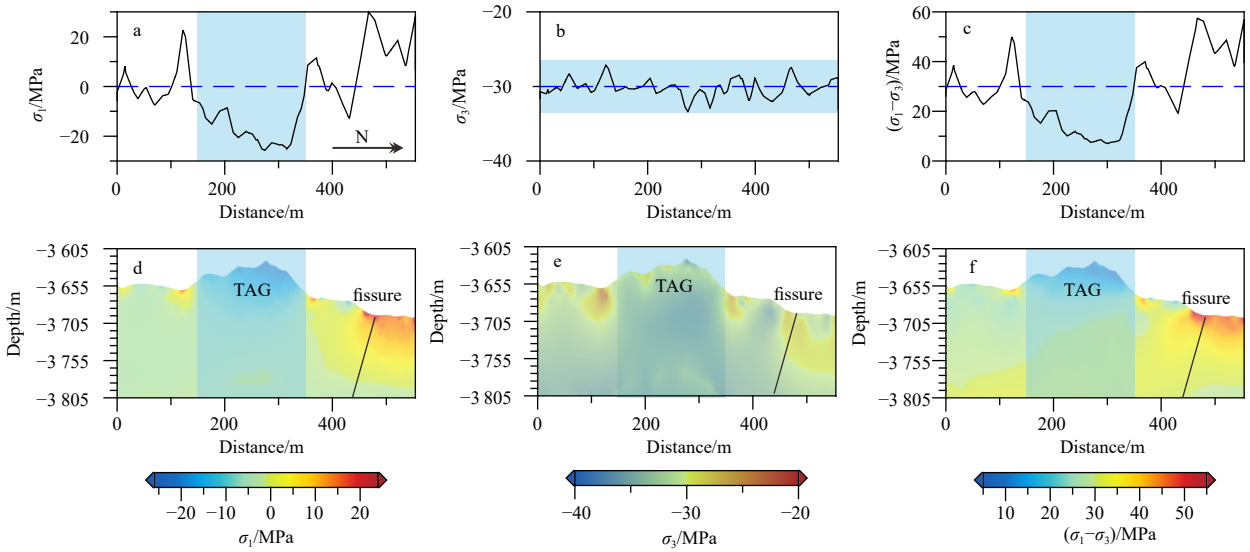

Fig. 4. Magnitudes of the principal stress σ_1 (a, d), the principal stress σ_3 (b, e), and the differential stress $\sigma_1-\sigma_3$ (c, f) in the S–N cross-section A–A′ of the TAG active hydrothermal mound.

(57.4 MPa) corresponds to the fissure, and the low differential stress zone (~7.5 MPa) corresponds to the mound (Figs 4c, f).

The stress state derived from Model B shows that both active and inactive hydrothermal mounds, as well as the Mir zone, are located in the zone that features a negative maximum horizontal stress σ_1 and relatively low differential stress $\sigma_1-\sigma_3$ (Fig. 5). In contrast, faults, fissures, and young NV zones seem to be associated with a positive maximum horizontal stress σ_1 and relatively high differential stress $\sigma_1-\sigma_3$, as shown in Fig. 5.

Profiles show the consistency of the stress state between the active mound and inactive mounds. The active TAG mound is located in the compressive stress zone and low differential stress zone, where σ_1 is less than –30 MPa and $\sigma_1-\sigma_3$ is less than 20 MPa (Fig. 6). The profile of the Southern inactive mound shows that the dome of the mound features a compressive stress regime and low differential stress (Fig. 7). The sections of the Shikai and Double mounds show similar stress states (Fig. 8), except with a decrease in the stress magnitudes. The magnitudes of the horizontal and differential stresses in the sections reveal that the tensile stress is primarily concentrated in faults and NV zones (Figs 6, 7 and 8), where the fault activity is predicted to be intense. The stress state of faults and NV zones is distinct from the SMS mounds (Fig. 9), both active and inactive mounds are characterized by lower differential stress and compressive stress, and the faults and NV zones are featured by higher differential stress and tensile stress.

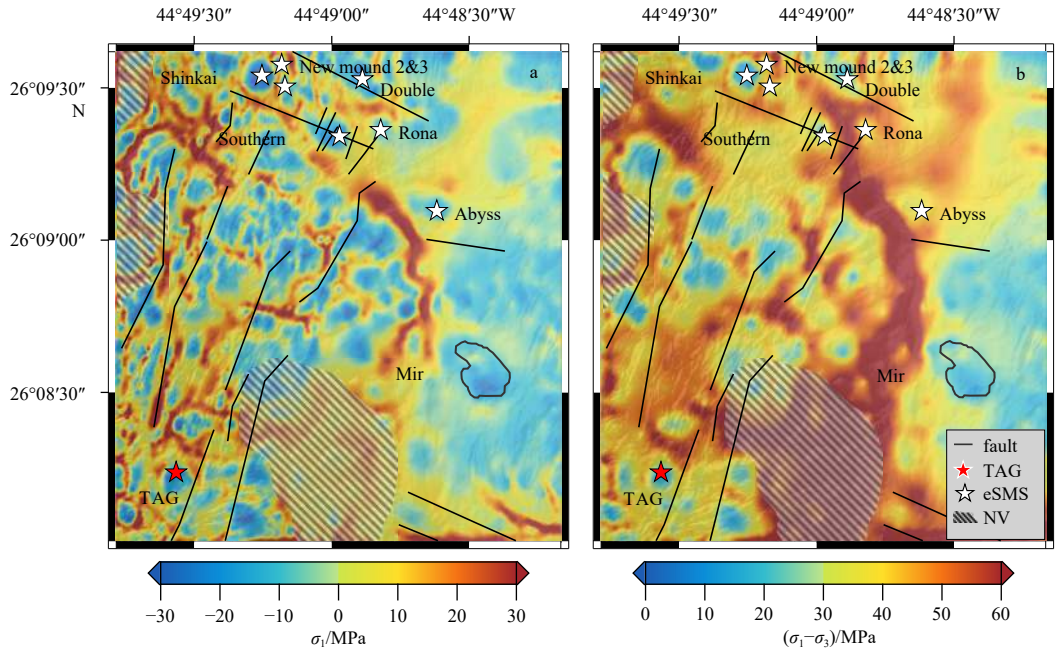

Fig. 5. Surface stress maps of the 3-D geological Model B of the TAG hydrothermal field. The principal stress σ_1 (a), and the differential stress $\sigma_1-\sigma_3$ (b).

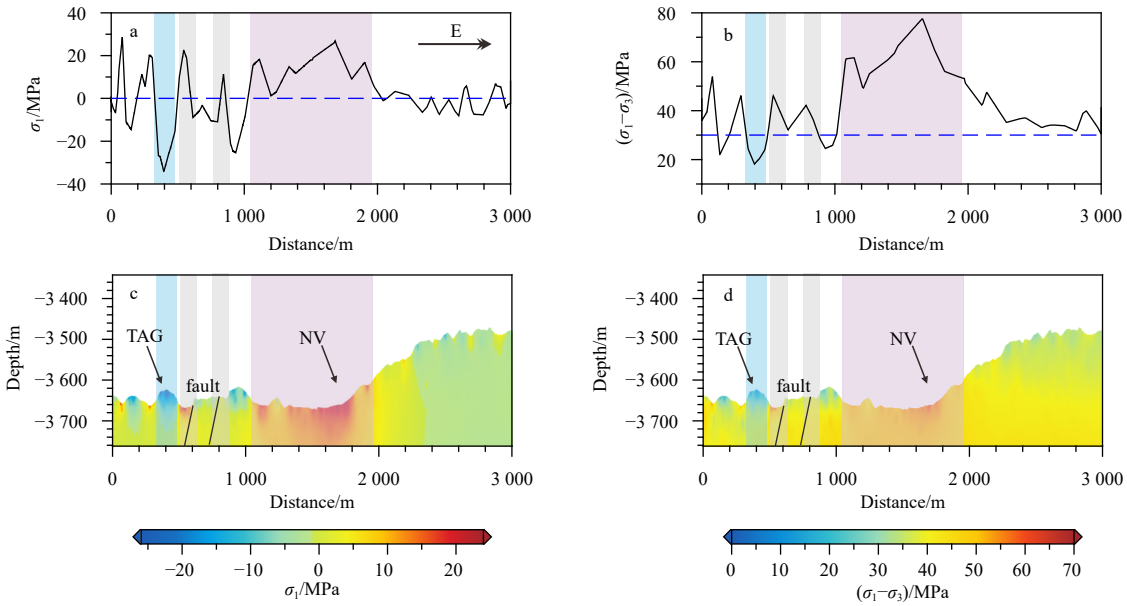

Fig. 6. Magnitudes of the principal stress σ_1 (a, c) and the differential stress $\sigma_1-\sigma_3$ (b, d) in the W–E cross-section B–B′ of the TAG hydrothermal field.

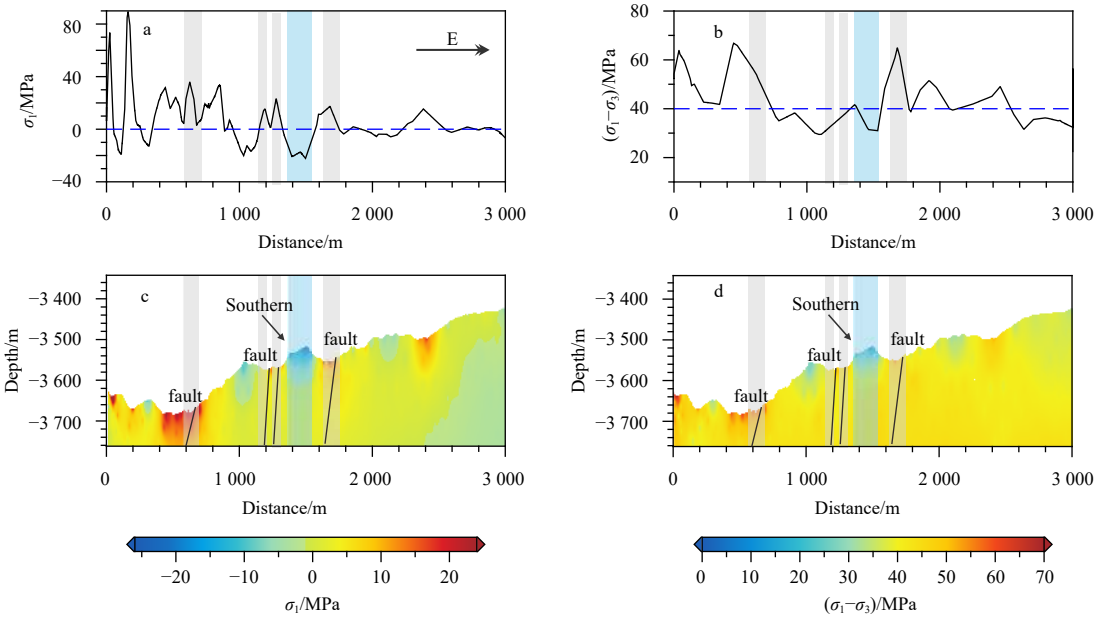

Fig. 7. Magnitudes of the principal stress σ_1 (a, c) and the differential stress $\sigma_1-\sigma_3$ (b, d) in the W–E cross-section C–C′ of the TAG hydrothermal field.

5 Discussion

5.1 *Formation of hydrothermal paths*

Although numerous studies have been conducted on the TAG hydrothermal field, knowledge of hydrothermal paths within the oceanic crust is very limited (Humphris et al., 2015). Geophysical surveys have revealed that primary circulation may be focused on detachment faults (deMartin et al., 2007), but the heat source is hypothesized to be distributed along a certain segment (Zhao et al., 2012). While high-temperature fluids are discharged through the summit of the active TAG mound, the flow is dispersed in the platform, and anhydrite precipitates in the intersecting sets of faults and fissures (Humphris and Kleinrock, 1996; Pontbriand and Sohn, 2014; Humphris et al., 2015). These features reveal that there are hydrothermal paths within shallow oceanic crust for venting high-temperature fluids and entraining seawater into the mound. Fissuring near the active TAG hydrothermal mound is due to tensile stress, with fissure widths ranging from 0.15 m to 3.5 m (Bohnenstiehl and Kleinrock, 2000). The depth of reaction-driven cracking is <150 m (Pontbriand and Sohn, 2014), and the tensile stress of fissure formation is estimated with Eq. (3).

$$\sigma = \frac{\left(\frac{G}{(1-\nu)}\right)(w/2)}{Z_0}. \tag{3}$$

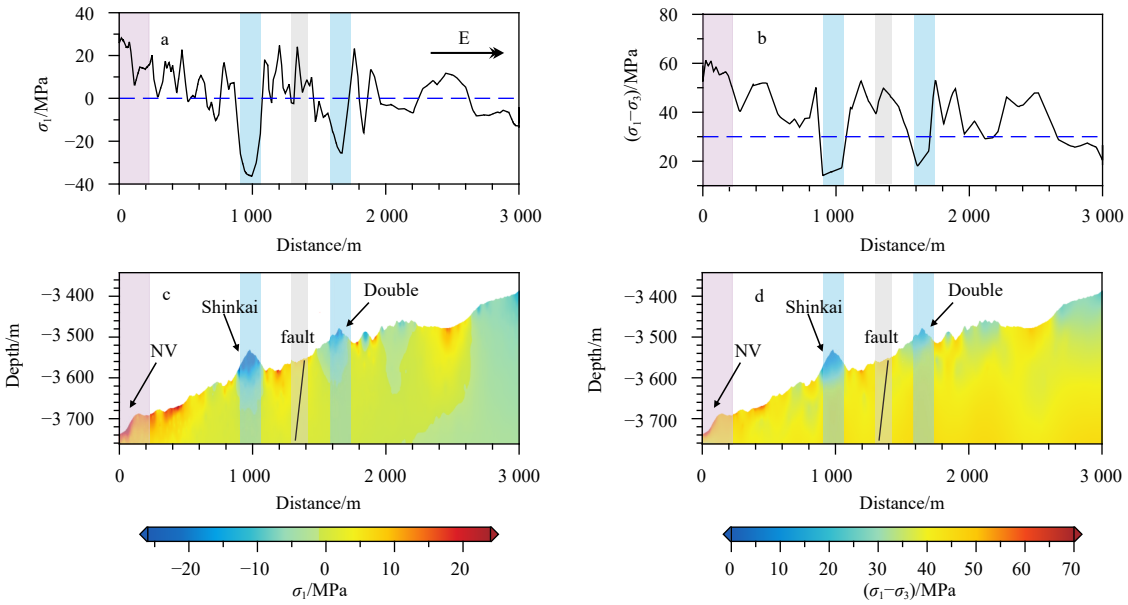

Fig. 8. Magnitudes of the principal stress σ_1 (a, c) and the differential stress $\sigma_1-\sigma_3$ (b, d) in the W–E cross-section D–D′ of the TAG hydrothermal field.

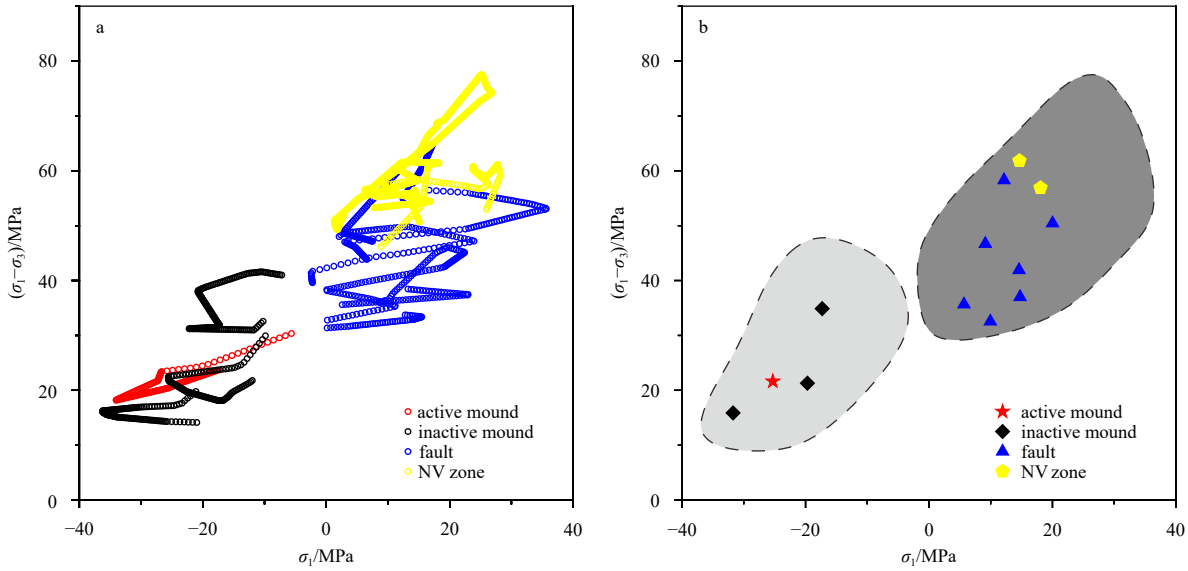

Fig. 9. Variations in maximum horizontal stress vs. differential stress. The data a were sampled from SMS mounds, faults, and NV zone, as shown in Figs 6, 7 and 8 (a). The grey dashed lines in b define a zone with compressive and low fault activity stress pattern, the dark grey area b represents tensile stress state and intense fault activity stress pattern.

Using the values of the static shear modulus G, Poisson's ratio ν, fissure width w and fissure depth Z_0 outlined in Table 2 (Wright et al., 1995; Wright, 1998; Pontbriand and Sohn, 2014), we estimate that the tensile stress ranges from 3.85 MPa to 90.06 MPa, consistent with the stress state of the fault and NV zone derived from our models, which is higher than the tensile strength (~1–6 MPa) in a volcanic rift zone environment (Haimson and Rummel, 1982). Fissures near the TAG mound are partially rubble-filled and initiate within the tensile stress field (Bohnenstiehl and Kleinrock, 2000), as Figs 3a and 5a show that fissures and faults are associated with the positive maximum horizontal stress σ_1, representing the tensile stress field. The intersections of

Table 2. Parameters used to estimate tensile stress (Wright et al., 1995; Wright, 1998; Pontbriand and Sohn, 2014)

Variable	Symbol	Value utilized	Reference
Static shear modulus/MPa	G	3 400±1 000	Wright et al. (1995)
Poisson's ratio	ν	0.43	Wright et al. (1995)
Fissure width/m	w	0.15–3.5	Bohnenstiehl and Kleinrock (2000)
Fissure depth/m	Z_0	<150	Pontbriand and Sohn (2014)

faults and fissures control hydrothermal activity (Kleinrock and Humphris, 1996), and tensile stress drives the formation and propagation of fractures, serving as hydrothermal paths.

Near-seafloor magnetic data indicate that there are inclined hydrothermal conduits beneath these SMS mounds of the TAG hydrothermal field, which may have undergone tectonic tilt (Szitkar et al., 2019). Hydrothermal fluid ascent is focused along the conduits, and the degassing and high-temperature anomalies coincident with the low compressive stress values suggest that the stress field controls the occurrence of fumaroles (Schöpa et al., 2011). Furthermore, the low-value zone of the maximum horizontal principal stress is considered the location of hydrothermal fluid discharge in the active TAG mound (Chen et al., 2017). Reservoirs derive overpressure and sustain hydrothermal activity, and individual mounds are linked by the same underlying hydrothermal permeability structure (Sohn et al., 2009; Jamieson and Gartman, 2020). Observations of flow-induced ground surface deformation imply that there are fluid subreservoirs distributed beneath the hydrothermal field, with overpressures ranging from several kPa to several MPa (Sohn et al., 2009). Given a compressive stress condition, if the overpressure is stronger than the interlayer differential stress, hydraulic fractures tend to grow vertically (Chen et al., 2020). This mechanism might account for the formation of vertically hydrothermal conduits. Figures 3a and 5a show that the active TAG mound and eSMS mounds are located in the region of negative maximum horizontal stress σ_1. In addition, Fig. 9 shows that these SMS mounds are characterized by a compressive stress state and low differential stress, supporting the former assumption that the formation of hydrothermal conduits is jointly controlled by differential stress and horizontal compressive stress.

5.2 *Implications for permeability*

The hydrothermal circulation of the active TAG mound and eSMS mounds can be activated by seawater penetrating through the hanging wall of the detachment fault with high permeability, which is enhanced by fault activity (Tivey et al., 2003). Numerical simulation results show that the occurrence, material flux, and mineral precipitation associated with hydrothermal activity correspond to the permeability of the oceanic crust (Germanovich et al., 2000; Marjanović et al., 2019; Guo et al., 2020). Furthermore, the permeability of serpentinites from the Mid-Atlantic Ridge demonstrates a decreasing trend with increasing differential stress (Falcon-Suarez et al., 2017). The dependence of permeability on stress suggests that the stress field can, to some extent, change the permeability of oceanic crust, which is one of the main controlling factors for hydrothermal circulation (Marjanović et al., 2019). Therefore, in the homogeneous basaltic oceanic crust, the permeability of the low differential stress region may be higher than that in other regions. In our homogeneous models, the active TAG hydrothermal mound and inactive mounds are located in the predicted high-permeability region, which is dominated by the low-differential-stress region (Figs 3b and 5b).

Additionally, fault activity is related to the differential stress $\sigma_1-\sigma_3$ (Zhu et al., 2015; Wang et al., 2017), and the fault and NV zone are located in the-high-differential-stress region (Figs 3b and 5b), implying that tectonic activity might be intensive. Seafloor morphology shows that the TAG hydrothermal field mainly consists of faulted volcanic rocks (Szitkar et al., 2019), fault and fissure groups represent different stress regimes, and tectonic processes occur during the evolution of the TAG hydrothermal field (Graber et al., 2020). The high-differential-stress region represents the potential for intensive tectonic activity, which forms a fault and NV zone (Fig. 9). Cracks in the rock could propagate downwards by thermoelastic stress (Olive and Crone, 2018), providing highly permeable paths for seawater penetration. In addition, the positive maximum horizontal stress σ_1 may be sufficient to induce and reopen cracks in shallow seafloor. The permeable structure of the TAG hydrothermal field is induced by the regional stress field, and its permeability is assumed to depend on the stress regime.

5.3 *Model limitations*

The geomechanical numerical models are designed as double-layer homogeneous elastic materials, ignoring the geological heterogeneity caused by tectonic processes and hydrothermal alteration. The thickness of the upper altered oceanic crust is estimated from the depth of the cracks and crustal velocity model instead of the observed lithology. According to the velocity model (Murton et al., 2019), the properties of the material are modified from those of oceanic basement rocks in the Mid-Atlantic Ridge (Hyndman and Drury, 1976). Tectonic and magmatic features, including block tilting and hot gabbro plutons (Zhao et al., 2012; Szitkar et al., 2019), are not considered in the model setup. Therefore, we focus on the stress field control of hydrothermal paths within the upper altered basaltic crust, and the stress field consists of ridge push force and body force, consistent with previous studies (Schöpa et al., 2011; Reiter and Heidbach, 2014; Hergert et al., 2015).

The calibration of models is based on the pressure of the overlying water column, without considering information of the crustal stress field. Although a multistage 3-D stress field modelling approach has been developed to overcome the limitation of insufficient stress data, the model's reliability still depends on the stress data (Ziegler et al., 2016). Stress information, including magnitude and orientation, is significant for model calibration, using the geological convention that the principal stress σ_3 is vertical and calculated with Eq. (2), the calibration of our models is reliable. Numerical simulation of the stress field would be greatly facilitated by technical methods to obtain the *in situ* stress state, and the WSM project is pursuing this effort (Heidbach et al., 2018).

6 Conclusions

In the present study, we established two geomechanical numerical models to simulate the stress field of the active TAG mound and TAG hydrothermal field. Comparing the results in the locations of SMS mounds, faults, and NV zones, the modelling results indicate a relation between the stress field and hydrothermal paths. The SMS mounds feature compressive and low differential stress regimes, and we assumed that the formation of hydrothermal conduits beneath mounds is controlled by the horizontal maximum stress and differential stress. However, faults and fissures are formed mainly in the tensile stress zone, where the horizontal maximum stress is positive. In addition, the high differential stress may induce intensive fault activity, providing cracks for seawater penetration. Furthermore, the permeability dependence on stress implies that the permeable structure is associated with the stress magnitude in the homogeneous model. These SMS mounds and Mir zone are located in the region of low stress, revealing the control of the stress field on the hydrothermal path.

In conclusion, the fluid paths for the secondary hydrothermal circulation system consist of faults and fissures within the shallow crust, and we presume that there are two mechanisms of path formation. The cracks that allow seawater penetration are

induced by tensile stress and intensified by high differential stress. The hydrothermal conduits for ascending fluid are controlled by compressive stress and low differential stress. In addition, the permeability stress sensitivity strengthens the influence of the stress field on the hydrothermal paths. These stress field features might be preferred targets for SMS deposits.

Acknowledgements

We are grateful to the scientific party of the cruise M127 for collecting data. The bathymetric data collection was supported by the R/V *Meteor* and the GEOMAR AUV team. We are also grateful to two anonymous reviewers for their constructive comments and suggestions.

References

Adelinet M, Fortin J, Schubnel A, et al. 2013. Deformation modes in an Icelandic basalt: From brittle failure to localized deformation bands. Journal of Volcanology and Geothermal Research, 255: 15–25, doi: 10.1016/j.jvolgeores.2013.01.011

Bohnenstiehl D R, Kleinrock M C. 2000. Fissuring near the TAG active hydrothermal mound, 26°N on the mid-Atlantic ridge. Journal of Volcanology and Geothermal Research, 98(1–4): 33–48, doi: 10.1016/S0377-0273(99)00192-4

Carruthers D, Cartwright J, Jackson M P A, et al. 2013. Origin and timing of layer-bound radial faulting around North Sea salt stocks: new insights into the evolving stress state around rising diapirs. Marine and Petroleum Geology, 48: 130–148, doi: 10.1016/j.marpetgeo.2013.08.001

Chen Qinzhu, Tao Chunhui, Liao Shili, et al. 2017. Analyzing the gravitational stress field to forecast hydrothermal field-a case study of TAG hydrothemal field. Haiyang Xuebao (in Chinese), 39(1): 46–51

Chen Ming, Zhang Shicheng, Xu Yun, et al. 2020. A numerical method for simulating planar 3D multi-fracture propagation in multi-stage fracturing of horizontal wells. Petroleum Exploration and Development, 47(1): 171–183, doi: 10.1016/S1876-3804(20)60016-7

Clair J S, Moon S, Holbrook W S, et al. 2015. Geophysical imaging reveals topographic stress control of bedrock weathering. Science, 350(6260): 534–538, doi: 10.1126/science.aab2210

deMartin B J, Sohn R A, Canales J P, et al. 2007. Kinematics and geometry of active detachment faulting beneath the trans-Atlantic Geotraverse (TAG) hydrothermal field on the Mid-Atlantic Ridge. Geology, 35(8): 711–714, doi: 10.1130/G23718A.1

Eshiet K I I, Welch M, Sheng Yong. 2018. Numerical modelling to predict fracturing rock (Thanet chalk) due to naturally occurring faults and fluid pressure. Journal of Structural Geology, 116: 12–33, doi: 10.1016/j.jsg.2018.07.021

Falcon-Suarez I, Bayrakci G, Minshull T A, et al. 2017. Elastic and electrical properties and permeability of serpentinites from Atlantis massif, mid-Atlantic ridge. Geophysical Journal International, 211(2): 686–699, doi: 10.1093/gji/ggx341

German C R, Petersen S, Hannington M D. 2016. Hydrothermal exploration of mid-ocean ridges: where might the largest sulfide deposits be forming?. Chemical Geology, 420: 114–126

Germanovich L N, Lowell R P, Astakhov D K. 2000. Stress-dependent permeability and the formation of seafloor event plumes. Journal of Geophysical Research: Solid Earth, 105(B4): 8341–8354, doi: 10.1029/1999JB900431

Graber S, Petersen S, Yeo I, et al. 2020. Structural control, evolution, and accumulation rates of massive sulfides in the TAG hydrothermal field. Geochemistry, Geophysics, Geosystems, 21(9): e2020GC009185, doi: 10.1029/2020GC009185

Grant H L J, Hannington M D, Petersen S, et al. 2018. Constraints on the behavior of trace elements in the actively-forming TAG deposit, Mid-Atlantic Ridge, based on LA-ICP-MS analyses of pyrite. Chemical Geology, 498: 45–71, doi: 10.1016/j.chemgeo.2018.08.019

Grevemeyer I, Reston T J, Moeller S. 2013. Microseismicity of the Mid-Atlantic Ridge at 7°S-8°15′S and at the Logatchev Massif oceanic core complex at 14°40′N-14°50′N. Geochemistry, Geophysics, Geosystems, 14(9): 3532–3554

Griffith W A, Becker J, Cione K, et al. 2014. 3D topographic stress perturbations and implications for ground control in underground coal mines. International Journal of Rock Mechanics and Mining Sciences, 70: 59–68, doi: 10.1016/j.ijrmms.2014.03.013

Guo Zhikui, Rüpke L H, Fuchs S, et al. 2020. Anhydrite-assisted hydrothermal metal transport to the ocean floor-insights from thermo-hydro-chemical modeling. Journal of Geophysical Research: Solid Earth, 125(7): e2019JB019035, doi: 10.1029/2019JB019035

Haimson B C, Rummel F. 1982. Hydrofracturing stress measurements in the Iceland research drilling project drill hole at Reydarfjordur, Iceland. Journal of Geophysical Research: Solid Earth, 87(B8): 6631–6649, doi: 10.1029/JB087iB08p06631

Hannington M, Jamieson J, Monecke T, et al. 2011. The abundance of seafloor massive sulfide deposits. Geology, 39(12): 1155–1158, doi: 10.1130/G32468.1

Heidbach O, Rajabi M, Cui Xiaofeng, et al. 2018. The World Stress Map database release 2016: Crustal stress pattern across scales. Tectonophysics, 744: 484–498, doi: 10.1016/j.tecto.2018.07.007

Hergert T, Heidbach O. 2011. Geomechanical model of the Marmara Sea region-II. 3-D contemporary background stress field. Geophysical Journal International, 185(3): 1090–1102, doi: 10.1111/j.1365-246X.2011.04992.x

Hergert T, Heidbach O, Reiter K, et al. 2015. Stress field sensitivity analysis in a sedimentary sequence of the Alpine foreland, northern Switzerland. Solid Earth, 6(2): 533–552, doi: 10.5194/se-6-533-2015

Hu Panpan, Yang Fengli, Tian Lixin, et al. 2019. Stress field modelling of the Late Oligocene tectonic inversion in the Liaodong Bay Subbasin, Bohai Bay Basin (northern China): Implications for geodynamics and petroleum accumulation. Journal of Geodynamics, 126: 32–45, doi: 10.1016/j.jog.2019.01.003

Humphris S E, Kleinrock M C. 1996. Detailed morphology of the TAG Active Hydrothermal Mound: Insights into its formation and growth. Geophysical Research Letters, 23(23): 3443–3446, doi: 10.1029/96GL03079

Humphris S E, Tivey M K, Tivey M A. 2015. The trans-Atlantic Geotraverse hydrothermal field: A hydrothermal system on an active detachment fault. Deep-Sea Research Part II: Topical Studies in Oceanography, 121: 8–16, doi: 10.1016/j.dsr2.2015.02.015

Hyndman R D, Drury M J. 1976. The physical properties of oceanic basement rocks from deep drilling on the Mid-Atlantic Ridge. Journal of Geophysical Research, 81(23): 4042–4052, doi: 10.1029/JB081i023p04042

Jamieson J W, Gartman A. 2020. Defining active, inactive, and extinct seafloor massive sulfide deposits. Marine Policy, 117: 103926, doi: 10.1016/j.marpol.2020.103926

Kleinrock M C, Humphris S E. 1996. Structural control on sea-floor hydrothermal activity at the TAG active mound. Nature, 382(11): 149–153

Koschinsky A, Heinrich L, Boehnke K, et al. 2018. Deep-sea mining: interdisciplinary research on potential environmental, legal, economic, and societal implications. Integrated Environmental Assessment and Management, 14(6): 672–691, doi: 10.1002/ieam.4071

Marjanović M, Barreyre T, Fontaine F J, et al. 2019. Investigating fine-scale permeability structure and its control on hydrothermal activity along a fast-spreading ridge (the East Pacific Rise, 9°43′-53′N) using seismic velocity, Poroelastic response, and numerical modeling. Geophysical Research Letters, 46(21): 11799–11810, doi: 10.1029/2019GL084040

McGregor B A, Harrison C G A, Lavelle J W, et al. 1977. Magnetic anomaly patterns on Mid-Atlantic Ridge crest at 26°N. Journal of Geophysical Research, 82(2): 231–238, doi: 10.1029/JB082i002p00231

Moon S, Perron J T, Martel S J, et al. 2020. Present-day stress field influences bedrock fracture openness deep into the subsurface. Geophysical Research Letters, 47(23): e2020GL090581, doi:

10.1029/2020GL090581
Murton B J, Lehrmann B, Dutrieux A M, et al. 2019. Geological fate of seafloor massive sulphides at the TAG hydrothermal field (Mid-Atlantic Ridge). Ore Geology Reviews, 107: 903–925, doi: 10.1016/j.oregeorev.2019.03.005
Olive J A, Crone T J. 2018. Smoke without fire: how long can thermal cracking sustain hydrothermal circulation in the absence of magmatic heat?. Journal of Geophysical Research: Solid Earth, 123(6): 4561–4581
Petersen S. 2019. Bathymetric data products from AUV dives during METEOR cruise M127 (TAG Hydrothermal Field, Atlantic). PANGAEA, https://doi.org//10.1594/PANGAEA.899415[2021-01-10]
Petersen S, Krätschell A, Augustin N, et al. 2016. News from the seabed-geological characteristics and resource potential of deep-sea mineral resources. Marine Policy, 70: 175–187, doi: 10.1016/j.marpol.2016.03.012
Pontbriand C W, Sohn R A. 2014. Microearthquake evidence for reaction-driven cracking within the Trans-Atlantic Geotraverse active hydrothermal deposit. Journal of Geophysical Research: Solid Earth, 119(2): 822–839, doi: 10.1002/2013JB010110
Rajabi M, Heidbach O, Tingay M, et al. 2017. Prediction of the present-day stress field in the Australian continental crust using 3D geomechanical-numerical models. Australian Journal of Earth Sciences, 64(4): 435–454, doi: 10.1080/08120099.2017.1294109
Reiter K, Heidbach O. 2014. 3-D geomechanical-numerical model of the contemporary crustal stress state in the Alberta Basin (Canada). Solid Earth, 5(2): 1123–1149, doi: 10.5194/se-5-1123-2014
Schöpa A, Pantaleo M, Walter T R. 2011. Scale-dependent location of hydrothermal vents: Stress field models and infrared field observations on the Fossa Cone, Vulcano Island, Italy. Journal of Volcanology and Geothermal Research, 203(3–4): 133–145, doi: 10.1016/j.jvolgeores.2011.03.008
Sleep N H. 1991. Hydrothermal circulation, anhydrite precipitation, and thermal structure at ridge axes. Journal of Geophysical Research: Solid Earth, 96(B2): 2375–2387, doi: 10.1029/90JB02335
Slim M, Perron J T, Martel S J, et al. 2015. Topographic stress and rock fracture: a two-dimensional numerical model for arbitrary topography and preliminary comparison with borehole observations. Earth Surface Processes and Landforms, 40(4): 512–529, doi: 10.1002/esp.3646
Sohn R A, Thomson R E, Rabinovich A B, et al. 2009. Bottom pressure signals at the TAG deep-sea hydrothermal field: evidence for short-period, flow-induced ground deformation. Geophysical Research Letters, 36(19): L19301, doi: 10.1029/2009GL040006
Szitkar F, Dyment J, Petersen S, et al. 2019. Detachment tectonics at Mid-Atlantic Ridge 26°N. Scientific Reports, 9(1): 11830, doi: 10.1038/s41598-019-47974-z
Tivey M K. 2007. Generation of seafloor hydrothermal vent fluids and associated mineral deposits. Oceanography, 20(1): 50–65, doi: 10.5670/oceanog.2007.80
Tivey M A, Schouten H, Kleinrock M C. 2003. A near-bottom magnetic survey of the Mid-Atlantic Ridge axis at 26°N: implications for the tectonic evolution of the TAG segment. Journal of Geophysical Research: Solid Earth, 108(B5): 2277, doi: 10.1029/2002JB001967
Wang Ke, Zhang Huiliang, Zhang Ronghu, et al. 2017. Analysis and numerical simulation of tectonic stress field in the Dabei gas field, Tarim basin. Acta Geologica Sinica, 91(11): 2557–2572
White S N, Humphris S E, Kleinrock M C. 1998. New Observations on the distribution of past and present hydrothermal activity in the TAG area of the mid-Atlantic ridge (26°08′N). Marine Geophysical Researches, 20(1): 41–56, doi: 10.1023/A:1004376229719
Wright D J. 1998. Formation and development of fissures at the East Pacific Rise: Implications for faulting and magmatism at mid-ocean ridges. In: Buck W R, Delaney P T, Karson J A, et al., eds. Faulting and Magmatism at Mid-Ocean Ridges. Washington: American Geophysical Union, 137–151
Wright D J, Haymon R M, MacDonald K C. 1995. Breaking new ground: estimates of crack depth along the axial zone of the East Pacific Rise (9°12′–54′N). Earth and Planetary Science Letters, 134(3–4): 441–457, doi: 10.1016/0012-821X(95)00081-M
Zhao Minghui, Canales J P, Sohn R A. 2012. Three-dimensional seismic structure of a Mid-Atlantic Ridge segment characterized by active detachment faulting (Trans-Atlantic Geotraverse, 25°55′N–26°20′N). Geochemistry, Geophysics, Geosystems, 13(11): 2012GC004454, doi: 10.1029/2012GC004454
Zhu Aiyu, Zhang Dongning, Jiang Changsheng. 2015. Numerical simulation of the segmentation of the stress state of the Anninghe-Zemuhe-Xiaojiang faults. Science China Earth Sciences, 59(2): 384–395
Ziegler M O, Heidbach O, Reinecker J, et al. 2016. A multi-stage 3-D stress field modelling approach exemplified in the Bavarian Molasse Basin. Solid Earth, 7(5): 1365–1382, doi: 10.5194/se-7-1365-2016